Synthesis and Experimental Validation of Battery Aging Test Profiles Based on Real-World Duty Cycles for 48-V Mild Hybrid Vehicles

Zifan Liu, *Student Member, IEEE*, Simona Onori, *Senior Member, IEEE*, and Andrej Ivanco, *Member, IEEE*

***Abstract*—Electrified powertrains are gaining a larger market share thanks to stricter emission regulation requirements and customer preferences. Ranging from micro hybrid to all-electric powertrains, however, their success highly depends on satisfactory life-long performance of onboard energy storage systems. In order to guide the battery pack design and management, real-world representative cell aging tests are essential for a successful product development. Focusing on cycle aging, this study proposes a novel methodology based on Welch's power spectral density estimation to characterize real-world cell duty cycles and synthesize representative profiles for cell aging tests. A 48-V mild hybrid vehicle model is developed in MATLAB/Simulink to relate the real-world vehicle-level drive cycles to cell-level duty cycles. Compared to existing test profiles found in literature, the newly designed profiles take the impacts of road conditions and driver styles into consideration to account for real-world resemblance. Experimental aging test results with the proposed aging profiles on nickel manganese cobalt lithium-ion cells not only hint at the real-world aging scenarios, but also lay the foundation for future work such as aging modeling. Repeatability of testing results is also investigated in this study.**

***Index Terms*—Battery aging test, driving style, lithium-ion battery, lithium ion NMC chemistry, power spectral density estimation, real-world drive cycle, 48V mild hybrid vehicle.**

I. Introduction

SOCIETAL expectations for reducing petroleum consumption and greenhouse gas emission in the transportation sector have resulted in new regulations, such as the 54.5 MPG fleet-wide CAFE (Corporate Average Fuel Economy) requirement in the United States [1]. Despite continuous improvements in conventional powertrains, electrification has been widely adopted by manufacturers and accepted by consumers. As a result, significant improvements in fuel efficiency can be attained, and positive recognition of product reliability has been achieved, and additional electrification costs for low-to-medium degree of hybridization have been successfully restrained. Remaining challenges for future sustainable mobility lie in electric range anxiety and battery degradation across real-world usage. Conceptually, these challenges can be overcome with a combined understanding of real-world driving conditions and battery aging evolution. This paper focuses on incorporating knowledge from real-world driving activities into battery cycle aging testing at the cell level.

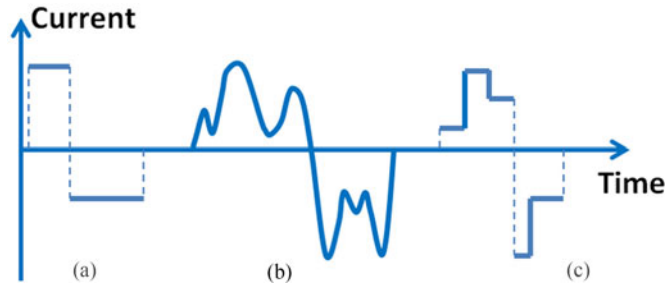

Fig. 1. Illustration of commonly used cycle aging test profiles.

Different from calendar aging tests which are usually controlled by temperature and SOC (State-of-Charge) [2]–[4], cycle aging tests incorporate additional stress factors, including ΔSOC, C-rate, Ah-throughput and discharge/charge events. The design of cycle aging tests is largely driven by the type of application, such as hybrid electric vehicles (HEVs), plug-in hybrid electric vehicles (PHEVs) and Electric Vehicles (EVs) [5]. Although battery cycle aging tests are being conducted worldwide, e.g., United States, Japan and Europe, a unified aging test protocol does not exist as different procedures are being used from country to country, especially concerning the test profiles.

This paper investigates battery operations in a 48V mild hybrid powertrain system [6], [7] and extracts useful information to synthesize repeatable test profiles to be run in laboratory settings. The cell cycle aging stress factors are closely linked to driver styles as well as road conditions. Nearly 2000 real-world drive cycles with detailed second-by-second speed traces are used in this study from a public travel survey provided by the National Renewable Energy Laboratory (NREL) [8].

Cycle aging test profiles from literature can be summarized into three categories. 1) *Constant current/power pulses*. These cycles, shown in Fig. 1(a), are widely used to separate the impacts of different stress factors, but usually with no implication from real-world scenarios [9]–[19]. 2) *Transient real-world cell duty cycles.* These transient traces, shown in Fig. 1(b), are directly adopted as test profiles to fully consider the

Manuscript received November 23, 2016; revised April 25, 2017; accepted June 9, 2017. Date of publication June 19, 2017; date of current version October 13, 2017. The review of this paper was coordinated by Dr. A. Chatterjee. *(Corresponding Author: A. Ivanco.)*

The authors are with the Department of Automotive Engineering, Clemson University, Greenville, SC 29607 USA (e-mail: zifanl@clemson.edu; sonori@clemson.edu; aivanco@clemson.edu).

Color versions of one or more of the figures in this paper are available online at http://ieeexplore.ieee.org.

Digital Object Identifier 10.1109/TVT.2017.2717187

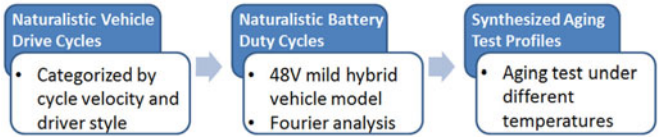

Fig. 2. Main steps describing the methodology developed in this paper to synthesize driver style-dependent aging cycles.

intrinsic cycle variability requiring complex statistical analysis to explore the correlation between aging phenomena and operating conditions [20], [21]. 3) *Semi-transient test profiles.* These cycles, as depicted in Fig. 1(c), which are usually synthesized from statistical analysis of real-world current/power profiles, are the most popular candidates for cycle aging campaigns [22]–[25], as they constitute a well-compromise between simplicity and real-world resemblance.

In this study, we propose a novel methodological framework to characterize real-world cell duty cycles in frequency domain by means of power spectral density (PSD) estimation, and synthesize them into representative *semi-transient test profiles.* Through our process, these output profiles are dynamic, charge-neutral, within manufacturer operation limits, and most importantly can be well traced back to the real-world driving scenarios. These representative profiles can be coupled with different temperatures to set up the aging test for aging assessment.

Energy storage systems for vehicle propulsion have evolved from lead-acid and nickel-metal-hydride to lithium-ion chemistry due to the improved energy and power density. Lithium-ion batteries further comprise a family of chemistries that employ mostly carbon-based anode and various cathode materials. Each provides disadvantages and advantages in several aspects: safety, performance, cost, specific energy, specific power and lifespan [26], [27]. The cycle aging experimental results conducted in this study aim at supplementing the understanding of lifespan of nickel-manganese-cobalt (NMC)-based cathode lithium-ion cells [12], [13]. Previous findings on other popular cathode materials, such as nickel-cobalt-aluminum (NCA) [10], [11], iron-phosphate (LFP) [14]–[16], and composite NMC-LMO [19], [25] can be found in the literature. The experimental results produced as part of this study can be applied to identify cell aging models, useful for the design and control of onboard lithium ion battery packs.

The paper is organized as illustrated in Fig. 2. In Section II, a detailed introduction of employed real-world driving data categorized by drive cycle mean speed and driving style is reported. Using the 48V mild hybrid vehicle model in MATLAB/Simulink, as presented in Section III, the vehicle-level drive cycles are battery cell duty cycles. The battery cell cycles are preprocessed, as discussed in Section IV, and analyzed in both frequency and time domains to attain their significant cyclic frequencies and current variance respectively, to facilitate construction of the sinusoidal characteristic test profiles, shown in Section V. Lastly, the aging experimental results with these profiles are reported and discussed regarding real-world driving and temperature variations in Section VI. Concluding remarks are given in Section VII.

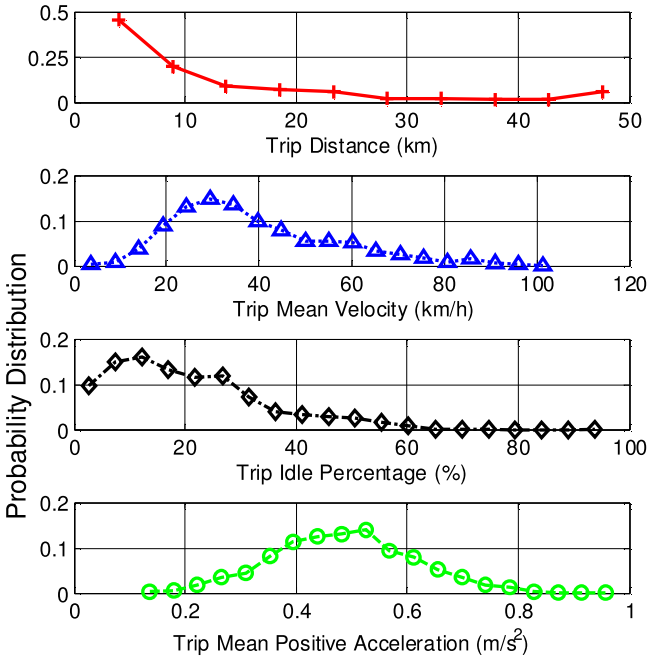

Fig. 3. Distribution of trip distance, trip mean velocity, trip idle percentage, trip mean positive acceleration in the SCAG naturalistic drive cycle database.

II. Real-World Driving Data

The drive cycle data source used in this study is part of a household travel survey from June 2001 to March 2002 conducted by SCAG (Southern California Association of Governments), of which de-identified data are publicly available through the U.S. Department of Energy's National Renewable Energy Laboratory (NREL) [8]. The raw data are recorded with 1 Hz sampling rate. After removing outlying vehicle speeds, speed spikes and infeasible accelerations, 1851 trips were adopted from 292 passenger vehicles with a total driven distance of about 25 000 km. The statistical distributions of the trip travel distance, mean velocity, idle percentage and mean positive acceleration rates are shown in Fig. 3. Drive cycles with driven distance less than 1 mile (1.6 km) are intentionally excluded.

A large variety of real-world driving activities are contained in this database. Mixing all driving data can lead to loss of interesting features of specific driving patterns, such as city driving with an aggressive driver. Hence, it is important to divide driving data into different categories based on selected cycle metrics. The driving conditions and driving style are chosen as categories in this study. Firstly, drive cycles are sorted by their mean speeds (low, medium and high) to indicate the driving conditions. Secondly, driving style for each trip is evaluated and classified as calm, normal and aggressive according to a metric from our previous study [6], [28]. In short, the metric defines the driving style in frequency domain as follows: 1) extract the jerk trace of each drive cycle as a second derivative of its speed trace; 2) calculate the periodogram as in Fig. 4 of the jerk trace given by the modulus squared of the Fast Fourier Transform (FFT) results in frequency domain; 3) attribute the low-frequency (LF) area to traffic conditions and high-frequency (HF) area to driver impacts in the periodogram; 4) multiply the power distribution

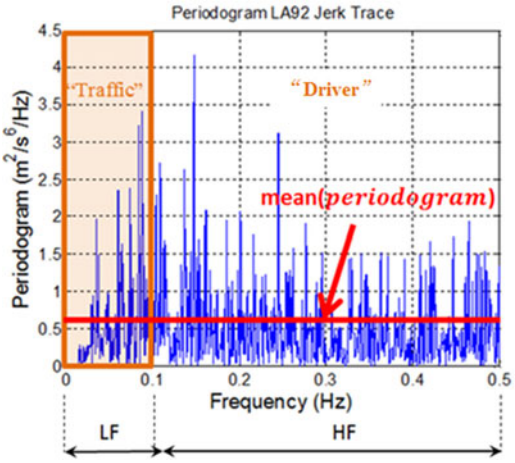

Fig. 4. LA92 drive cycle and driving style.

TABLE I
THE NUMBER OF REAL-WORLD TRIPS IN EACH CATEGORY

Number of Trips	Calm	Normal	Aggressive
Low Mean Speed (0∼29 km/h)	**64**	**235**	**318**
Medium Mean Speed (29∼43 km/h)	**150**	**234**	**233**
High Mean Speed (>43 km/h)	**406**	**141**	**70**

ratio in frequency domain, $\frac{HF}{HF+LF}$, by the average value of the periodogram, $mean(periodogram)$. The steps 3) and 4) take the frequency and magnitude of the jerk traces into account to quantify the driving style. The above process is explicitly defined by:

$$Driving\ style = mean\,(periodogram) * \frac{HF}{HF\ +\ LF} \quad (1)$$

Where, *mean(periodogram)* is the average value of the periodogram; *LF* is the power aggregated in the low frequency range by summing up the low frequency components below 0.1 Hz; *HF* is the power aggregated in the high frequency range by summing up the high frequency components above 0.1 Hz. The cutoff frequency for the separation of the traffic and driver activities is selected at 0.1 Hz for consistency, below which all trips have at least 99% of speed variance aggregated [6], [28].

Table I shows the number of trips in each category determined by drive cycle mean velocity and driving style aggressiveness, of which the probabilistic distributions are separated into three sets respectively (calm, normal, aggressive for driver styles; low, medium and high-speed for driving conditions), where each speed category contains 617 trips. While aggressive style dominates the low-speed driving, calm style rules the high-speed scenario. This interesting trend implies the real-world variability of driver behaviors.

III. 48-V MILD HYBRID VEHICLE

A 48-V mild hybrid propulsion system is typically based on a conventional powertrain where a starter-generator is coupled to the internal combustion engine via belt drive or by placing it directly on the engine shaft. Assuming parallel pre-transmission hybrid configuration, a generic 48V hybrid vehicle model is developed in Matlab/Simulink as schematically shown in Fig. 5 [6]. The specifications of engine, transmission, battery pack and starter-generator are summarized in Tables II and III.

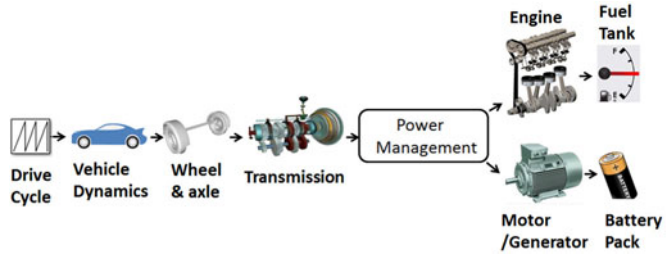

Fig. 5. A generic 48V mild hybrid vehicle configuration.

TABLE II
SPECIFICATIONS FOR VEHICLE/ENGINE/TRANSMISSION

Specifications	Units	Values
	Vehicle Dynamics	
Curb Weights	kg	1350
Passenger and Cargo Weight	kg	136
The Product of Drag Area and Drag Coefficient	m^2	0.66
Rolling Resistance Coefficient		0.012
Tire Radius	m	0.287
	Engine	
Engine Type		Inline 4 cylinders & Naturally aspirated & Spark Ignition
Engine Displacement	L	1.9
	Transmission	
Transmission Type		6-speed manual
Transmission Ratios		[4.148, 2.370, 1.756, 1.155, 0.859, 0.683]
Final Drive Ratio		3.21

The power management strategy implemented in the simulation is as follows: for positive power demands, large-amplitude but low-frequency components are sent to the engine as the base load and small-amplitude but high-frequency components are sent to the battery to balance the power peaks; the negative power demands are met in sequence by engine drag, battery charge power (for maximum regeneration) and by friction brakes. The battery power demands are further altered to achieve charge-sustaining behavior in the SOC window between 0.45 and 0.65. More details about the vehicle modeling approach can be found in [6].

For better illustration, an exemplary drive cycle and its related battery cell current profile are compared in Fig. 6. In contrast to charge current (negative), the discharge counterparts seldom reach the power limit but display a wide range of power demands and time durations. All drive cycles in the database can then be evaluated on the 48V hybrid vehicle model to obtain the trip-related cell current profiles. The next section identifies latent features in real-world battery duty cycles.

TABLE III
SPECIFICATIONS FOR BATTERY AND STARTER-GENERATOR

Specifications	Units	Values
	Battery	
Cell Chemistry		Nickel-Manganese-Cobalt (NMC) Lithium ion
Cell Nominal Voltage	V	3.6
Cell Rated Capacity	Ah	2.0
Cell Max Discharge Continuous Current	A	32
Cell Max Charge Continuous Current	A	12
Internal Impedance	mΩ	12 measured by AC1kHz
Battery Pack Configuration		14 series/4 parallel
	Starter-Generator (Brushless DC)	
Supply DC Voltage	V	42-58
Max/Continuous Power	kW	25/20
Max Torque	Nm	75 @ (0∼3000 rpm)
Max Speed	rpm	10000

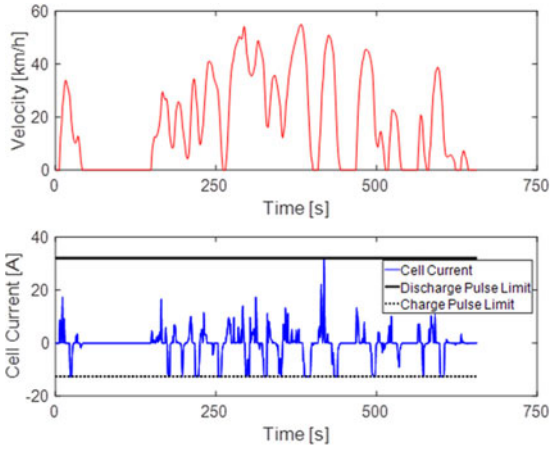

Fig. 6. A drive cycle speed profile drawn from the SCAG cycle database [8] and related battery cell current profile.

IV. REAL-WORLD BATTERY DUTY CYCLES ANALYSIS

Discharge and charge micro profiles are displayed in Fig. 7 representing an example of 460 s∼540 s time window from the current profile in Fig. 6. This study aims to investigate whether there are underlying cyclic patterns in discharge/charge micro profiles and how these patterns vary across real-world scenarios. While only sequential data are observed in time domain, cyclic events can be better captured in frequency domain with the Fourier analysis, while the zero current snippets during vehicle stops are not considered.

A. Introduction of Fourier Analysis

Discrete Fourier Transform (DFT) [29] can be applied to transform cell current profiles from time domain to frequency domain. Given a length-N signal, $x(n)$ in discrete time domain, with the Discrete Fourier Transform (DFT), the Fourier analysis

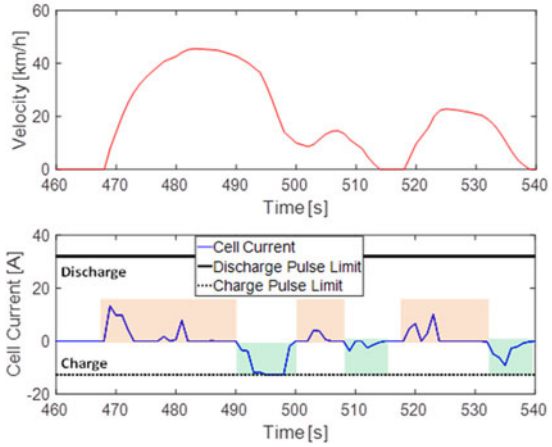

Fig. 7. The definition of discharge and charge micro profiles.

formula of the signal is in Equation (2):

$$X(k) = \sum_{n=0}^{N-1} x(n) W_N^{nk},\ k = 0, \ldots,\ N-1 \tag{2}$$

where $W_N = e^{-j\frac{2\pi}{N}}$.

Therefore, a finite length-N signal in time domain can be transformed to frequency domain and decomposed into a set of N sinusoidal oscillatory components, characterized by the $X(k)$ in frequency domain. $X(k)$, which contain the magnitude and initial phase of each oscillator, corresponds to the digital frequency of $\frac{2\pi k}{N}$ $(k = 0,\ 1,\ \ldots,\ N-1)$. It denotes the abstract dimensionless digital frequency as $\omega_{digital}$, it relates to real frequency f_{real} in Hertz as in Equation (3):

$$f_{real} = \frac{f_s}{2\pi}\omega_{digital} \tag{3}$$

where f_s is the sampling frequency of the signal.

Due to the phenomenon of *Aliasing* [29], the maximum real frequency for the signal is $f_s/2$ for a real-valued signal and f_s for a complex-valued signal. Since the speed values are all real and the sampling frequency is 1Hz for all available speed traces in this study, the real-frequency range should be (0: 1/N: 1/2).

The DFT produces a frequency spectrum which contains all information about the original time series. In other words, the original signal can be reconstructed by the Inverse Discrete Fourier Transfer (IDFT), or say, the Fourier synthesis, as illustrated in Equation (4) for above signal:

$$x(n) = \frac{1}{N}\sum_{k=0}^{N-1} X(k) W_N^{-nk},\ n = 0, \ldots,\ N-1 \tag{4}$$

DFT is a numerical tool which deals with finite signals and defines a finite number of operations, and the Fast Fourier Transform (FFT) is commonly used as the computation efficient algorithm to accelerate the DFT. There are several techniques to implement the FFT, such as the Cooley-Tukey algorithm [30].

While the FFT spectrum analysis preserves both the magnitude and phase of each frequency component in the form of a complex number, a common technique is to calculate the squared amplitude to estimate the so-called PSD. The simplest

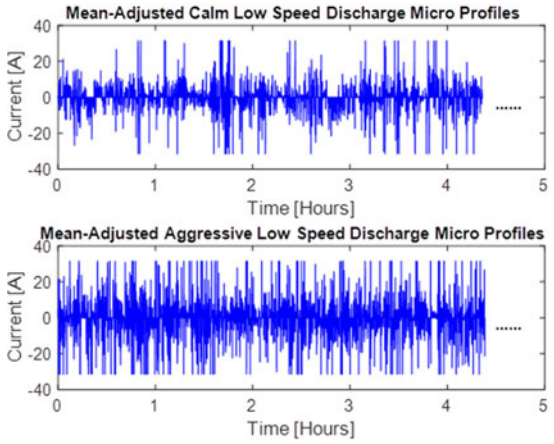

Fig. 8. Mean-adjusted concatenated discharge micro profiles of calm and aggressive low-speed trips (∼4.5 hour data for display).

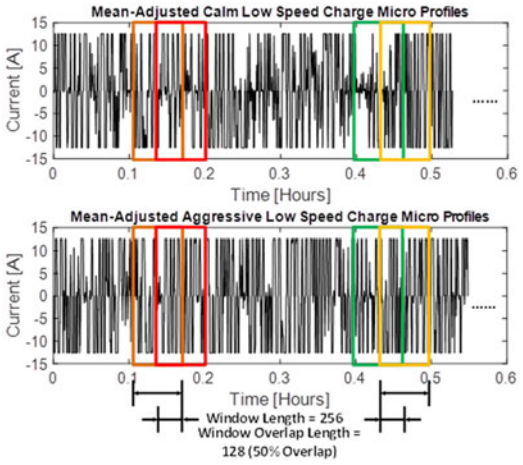

Fig. 9. Mean-adjusted concatenated charge micro profiles of calm and aggressive low-speed trips (∼0.5 hour data for display); also including illustration of Welch's moving window method for power spectral density estimation.

estimator is the periodogram by the modulus squared of the FFT, $\hat{\phi}_p$ as follows.

$$\hat{\phi}_p(k) = \frac{1}{N}\left|\sum_{n=0}^{N} x(n) W_N^{nk}\right|^2, \; k = 0, \ldots, N-1 \qquad (5)$$

However, despite its simplicity, the periodogram suffers from various drawbacks such as high spectral leakage, high variance and estimation inconsistency. While parametric techniques have been proposed to overcome the problems [29], the present study comprehensively considers several nonparametric candidates. These include, 1) modified periodogram which multiplies a time series with a specified window (Hamming window, Kaiser window, Blackman window, etc.) before calculating its periodogram; 2) Barlett's method which averages the periodograms of several segments of a time series; 3) Welch's method which averages the modified periodograms of several segments of a time series.

B. Application of Fourier Analysis

Discharge and charge micro profiles are treated separately. They are further concatenated in each driving data category. In addition, signal pre-processing steps, (i) deleting zero-current periods during vehicle stops, (ii) adjusting the mean values of the concatenated profiles by inversing the sign of every other micro profile, are executed to make PSD estimation results more discernable. The mean-adjusted discharge and charge data from calm and aggressive drivers are displayed in Figs. 8 and 9. Considering the length of data and accuracy requirement, we apply the Welch's method and illustrate the process specifically for the charge data in Fig. 9. A hamming window of length 256 is moving along the time series with an overlap of length 128; these modified periodograms are averaged to output the estimated PSDs in Figs. 10 and 11 for discharge and charge data under different driving conditions. The length 256 and 128 are chosen to achieve a satisfactory smoothing level.

As the PSD indicates the distribution of time series variance across the frequency domain, we emphasize the different peak values of PSDs between calm and aggressive drivers in

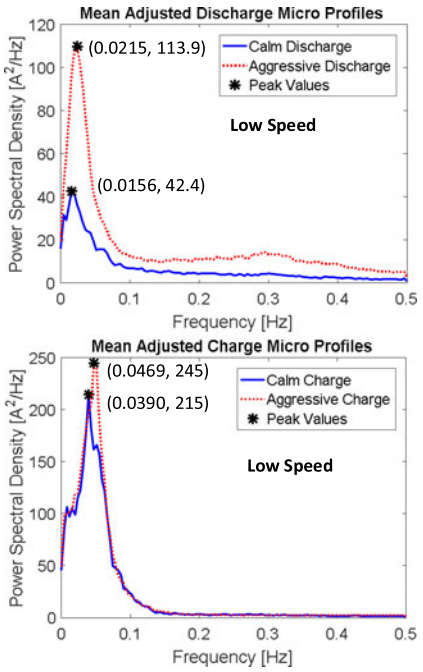

Fig. 10. Power spectral density estimation for low-speed drive cycles.

low-speed driving activities in Fig. 10. For illustration, in discharge, aggressive drivers have the peak frequency of 0.0215 Hz, translated to a 46-second sinusoidal period in time domain; calm drivers have the peak frequency of 0.0156 Hz, equal to a 64-second period. During charging, the comparison is 0.0469 Hz of aggressive to 0.0390 Hz of calm; equivalent to a period of 22-seconds to 26- seconds. These differences of peak frequencies are compiled in Table IV. The fact that aggressive drivers have shorter discharge/charge events applies as well for the high-speed driving activities. Since the concatenated charge data are much shorter than discharge data, the smoothing levels of their PSD estimations are worse as indicated by sporadic lower peaks in Fig. 11. Another difference is the area under the curve of PSDs, which is proportional to the variances of concatenated time series, compiled in Table V. The information in Tables IV and V can be summarized as:

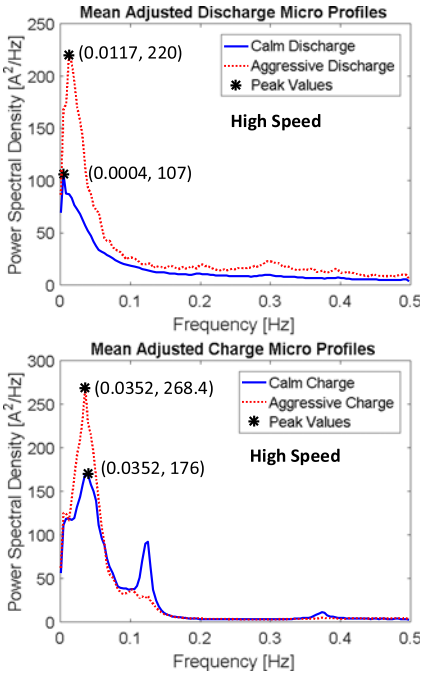

Fig. 11. Power spectral density estimation for high-speed drive cycles.

TABLE IV
SIGNIFICANT FREQUENCY OF CONCATENATED MEAN-ADJUSTED DISCHARGE AND CHARGE MICRO TRIPS FOR CALM AND AGGRESSIVE DRIVERS IN LOW/HIGH-SPEED DRIVE CYCLES

Peak Frequency (Hz)	Mean-Adjusted Discharge		Mean-Adjusted Charge	
	Calm	Aggressive	Calm	Aggressive
Low Speed	**0.0156 (64s)**	**0.0215 (46s)**	**0.0390 (26s)**	**0.0469 (22s)**
High Speed	**0.0004 (250s)**	**0.0117 (86s)**	**0.0352 (28s)**	**0.0352 (28s)**

TABLE V
VARIANCE OF CONCATENATED MEAN-ADJUSTED DISCHARGE AND CHARGE MICRO TRIPS FOR CALM AND AGGRESSIVE DRIVERS IN LOW/HIGH-SPEED DRIVE CYCLES

Variance (A^2)	Mean-Adjusted Discharge		Mean-Adjusted Charge	
	Calm	Aggressive	Calm	Aggressive
Low Speed	**22**	**55**	**74**	**82**
High Speed	**53**	**99**	**84**	**91**

1) The batteries of aggressive drivers switch faster between discharge and charge;
2) The batteries in low-speed driving conditions switch faster between discharge and charge;
3) In each category the charge periods are shorter than discharge counterparts;
4) The differences of current variances in discharge scenarios are significantly enlarged by both driving style aggressiveness and speed;

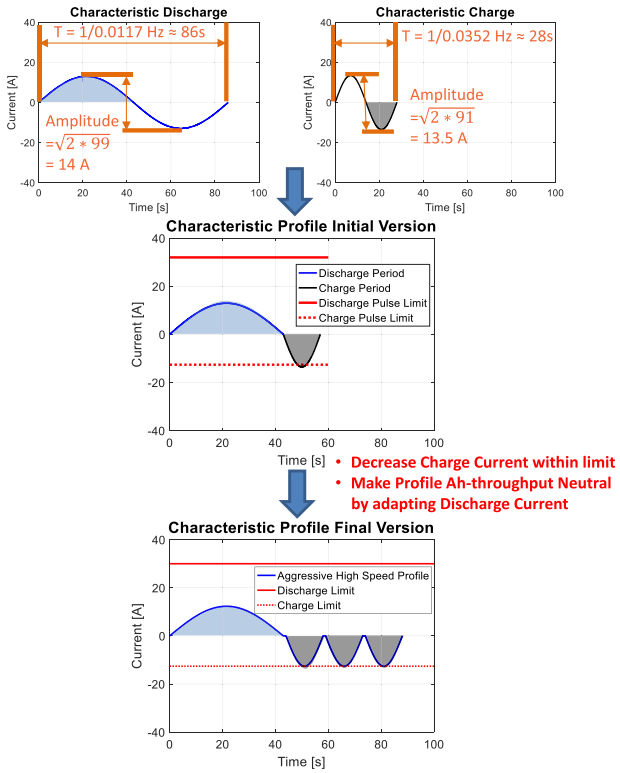

Fig. 12. The process of synthesizing the characteristic battery test profiles for aggressive high-speed category.

5) The differences of current variances in charge scenarios are relatively small because they are mostly saturated by the charge current limits.

V. SYNTHESIS OF BATTERY TEST PROFILES

Information on Tables IV and V are used to synthesize characteristic cell aging test profiles based on cycle speeds and driver style. The aging profiles are synthetized in the form of sinusoidal waves with the peak frequencies from estimated PSDs and the period of mean-adjusted time series. The derivation of such profiles is illustrated, see Fig. 12, considering the aggressive high-speed category. Constructed with half sinusoidal profiles separately from discharge and charge data, the synthesized characteristic profile should comply with cell current limits and must be Ah-throughput neutral to guarantee repeatability. The characteristic profiles for calm low-speed, calm high-speed, aggressive low-speed and aggressive high-speed driving conditions are compiled in Fig. 13. For all of them, the charge parts are close to the manufacturer's limit, but the discharge parts are significantly different in duration and current magnitude. Aggressive drivers tend to discharge their batteries faster and harder; while high-speed driving further increases battery discharge duration and current magnitude.

VI. EXPERIMENTAL SETUP AND AGING TEST RESULTS

This section discusses the experimental setup and the aging test results using the synthesized charge-neutral profiles developed in previous sections. Experiments were carried out at the

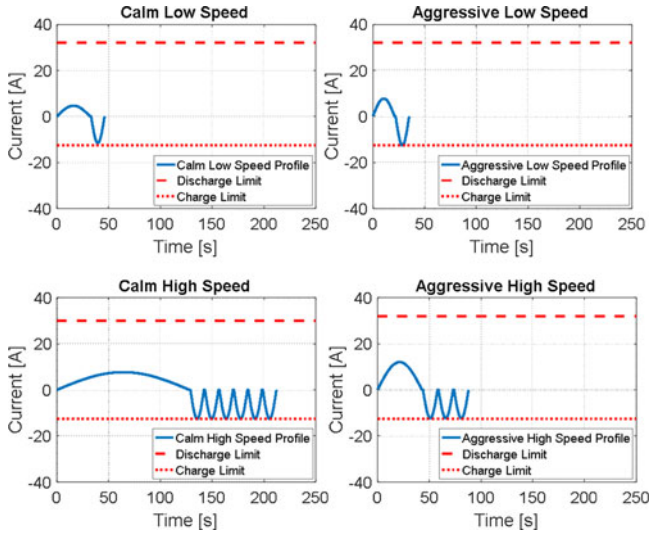

Fig. 13. Characteristic battery test profiles for four categories of driving data.

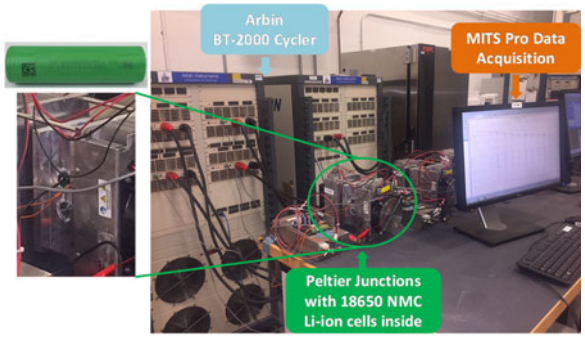

Fig.14. Experimental test set-up at the BACh Laboratory.

TABLE VI
AGING TEST MATRIX, NUMBERED CELLS WITH AGING CONDITIONS

Aging Conditions	Cell No. #
Calm Low Speed 23 °C (CLS23)	Cell 1 / Cell 2
Calm Low Speed 45 °C (CLS45)	Cell 3 / Cell 4
Aggressive High Speed 23 °C (AHS23)	Cell 5 / Cell 6
Aggressive High Speed 45 °C (AHS45)	Cell 7 / Cell 8

Battery Aging and Characterization (BACh) Laboratory at the Automotive Engineering Department at Clemson University. The experimental setup used for the aging campaign, shown in Fig. 14, is composed of the Arbin BT-2000 battery cycler with a programmable power supply and an electronic load; a MITS Pro data acquisition software for the programming of test profiles and the control of the Arbin cycler; and Peltier junctions that are in direct contact with the cell fixtures for thermoelectric temperature control. In this study we use the cylindrical 18650 NMC lithium ion cells, the detailed specifications of which can be found in Table III.

In the experimental aging campaign, two extreme conditions were considered: the calm low-speed (CLS) and aggressive high-speed (AHS). Both profiles were tested at two temperatures, 23 °C and 4 °C, respectively to form the test matrix shown in Table VI. For each test condition, two cells were

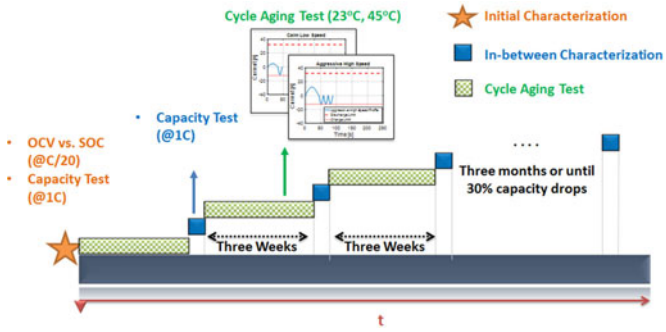

Fig.15. The flowchart of the aging test.

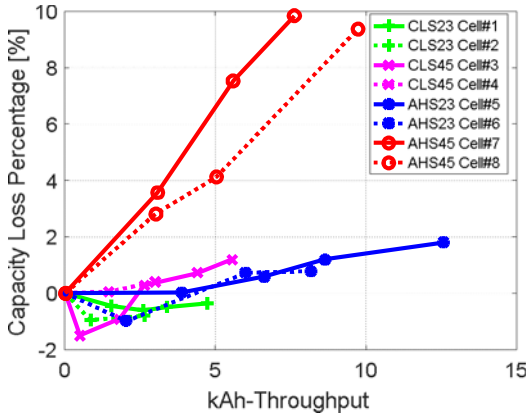

Fig.16. Battery aging test results with in-house characteristic profiles.

tested to check for repeatability. All cells underwent capacity characterization tests at room temperature of around 25 °C at the beginning and thereafter every three-week period. A flowchart of this aging campaign is shown in Fig. 15. The 1C capacity tests was performed by firstly charging the cell to 4.2 V at a constant current of 1 C, then holding constant voltage at 4.2 V until the current dropped to C/50. The fully charged cells were rested for one hour, then the 1 C discharge current was applied until the cut-off voltage of 2.5 V was reached.

The normalized capacity loss results from three-month characterization tests are shown in Fig. 16. For better comparison, the x-axis is in Ah-throughput rather than time. The cells undergoing the AHS45 cycle (i.e., cells #7 and #8) lost 10% of their initial capacity in only two months due to the severe aging rate of the cycle. Cells #1 and #2, undergoing the CLS23 cycle show no capacity loss after a three-month aging period. A slight capacity recovery is instead observed. Interestingly, for CLS45 Cell#3 and AHS23 Cell#6, some capacity recoveries are also observed during the first few aging characterization stages, different from their repeated counterparts.

The overall aging results can be interpreted as follows: 1) the impact of temperature on aging is more significant than the discharge current magnitude, or the driving style; 2) the impact of the rate of discharge on aging is larger at high temperature; 3) the impact of temperature on aging is larger as the discharge rate increases. The aging results derived from experimental testing validated the impact of the real-world driving on the cell aging properties, and emphasized the need for efficient battery thermal management, as well as the benefits one might obtain from eco-driving.

VII. Conclusion

This study analyzed real-world battery duty cycles to create synthesized characteristic aging test profiles. Using naturalistic vehicle drive cycles, which are categorized by mean speed and driving style, a 48-V mild hybrid vehicle model equipped with a power management strategy was constructed in /Simulink to generate real-world battery duty cycles. By adopting the Welch's PSD estimation method on discharge and charge data separately, we concluded that: 1) discharge pulses are generally longer in duration than charge pulses; 2) an aggressive driver style shortens the discharge/charge durations, while high-speed driving activities lengthen them; 3) aggressive driver style and high-speed driving activities both stimulate larger discharge/charge current rates. Characteristic sinusoidal test profiles were synthesized with peak frequencies and amplitudes respectively from PSD estimations and time series variances. Aging tests were performed using the current profiles designed to be within the manufacturers' current limits and Ah-throughput neutral. Applying different temperatures and "driving styles", the cycle aging results reveal the negative impacts on cell capacity loss from aggressive driver style at high temperature. The methodologies of this study for the characterization of real-world duty cycles and synthesis of representative profiles can be flexibly extended to new datasets. The aging test results lay the foundation for the cell aging modeling and the investigation of cycle aging mechanisms relative to the real-world usage. This study has also shown that repeatability of tests is an important aspect to account for consistency of test results.

Acknowledgment

The authors would like to acknowledge Johnson Controls Power Solutions for supporting this project, and especially Mike Andrew for overseeing our collaboration and Dr. Z. Jin for sharing her technical knowledge and providing valuable advice in order to increase the quality of this work. The author would also like to thank A. Allam for his help with the experimental battery testing is also acknowledged.

References

[1] National Highway Traffic Safety Administration, "Environmental protection agency, 2017 and later model year light-duty vehicle greenhouse gas emissions and corporate average fuel economy standards; final rule," Final Rule, [Online]. Available at http://www. nhtsa. gov/fue l-economy, accessed May 2, 2013.

[2] R. Spotnitz, "Simulation of capacity fades in lithium-ion batteries," *J. Power Sources*, vol. 113, no. 1, pp. 72–80, 2003.

[3] M. Kassem *et al.*, "Calendar aging of a graphite/LiFePO 4 cell," *J. Power Sources*, vol. 208, pp. 296–305, 2012.

[4] B. Stiaszny *et al.*, "Electrochemical characterization and post-mortem analysis of aged LiMn 2 O 4–NMC/graphite lithium ion batteries part II: Calendar aging," *J. Power Sources*, vol. 258, pp. 61–75, 2014.

[5] M. Conte, F. V. Conte, I. D. Bloom, K. Morita, T. Ikeya, and J. R. Belt, "Ageing testing procedures on lithium batteries in an international collaboration context," in *Proc. 25th World Battery, Hybrid Fuel Cell Elect. Vehicle Symp. Exhib.*, Nov. 2010, pp. 5–9.

[6] Z. Liu, A. Ivanco, and Z. S. Filipi, "Impacts of real-world driving and driver aggressiveness on fuel consumption of 48V mild hybrid vehicle," *SAE Int. J. Alternative Powertrains*, vol. 5, pp. 249–258, 2016.

[7] R. Anthony and B. Sisk, "A simulation based analysis of 12V and 48V microhybrid systems across vehicle segments and drive ycles," SAE Techn. Paper No. 2015-01-1151., 2015.

[8] National Renewable Energy Laboratory. Transportation Secure Data Center: [Online]. Available: www.nrel.gov/tsdc. (Accessed January 15, 2015).

[9] I. Bloom *et al.*, "An accelerated calendar and cycle life study of Li-ion cells," *J. Power Sources*, vol. 101, no. 2, pp. 238–247, 2001.

[10] R. G. Jungst *et al.*, "Accelerated calendar and pulse life analysis of lithium-ion cells," *J. Power Sources*, vol. 119, pp. 870–873, 2003.

[11] E. V. Thomas *et al.*, "Accelerated power degradation of Li-ion cells," *J. Power Sources*, vol. 124, no. 1, pp. 254–260, 2003.

[12] J. Schmalstieg, S. Käbitz, M. Ecker, and D. U. Sauer, "A holistic aging model for Li (NiMnCo) O 2 based 18650 lithium-ion batteries," *J. Power Sources*, vol. 257, pp. 325–334, 2014.

[13] S. Käbitz *et al.*, "Cycle and calendar life study of a graphite| LiNi 1/3 Mn 1/3 Co 1/3 O 2 Li-ion high energy system. Part A: Full cell characterization," *J. Power Sources*, vol. 239, pp. 572–583, 2013.

[14] Y. Zhang, C. Y. Wang, and X. Tang, "Cycling degradation of an automotive LiFePO 4 lithium-ion battery," *J. Power Sources*, vol. 196, no. 3, pp. 1513–1520, 2011.

[15] J. Wang *et al.*, "Cycle-life model for graphite-LiFePO 4 cells," *J. Power Sources*, vol. 196, no. 8, pp. 3942–3948, 2011.

[16] D. I. Stroe, M. Świerczyński, A. I. Stan, R. Teodorescu, and S. J. Andreasen, "Accelerated lifetime testing methodology for lifetime estimation of Lithium-ion batteries used in augmented wind power plants," *IEEE Trans. Ind. Appl.*, vol. 50, no. 6, pp. 4006–4017, Nov./Dec. 2014.

[17] M. Safari, M. Morcrette, A. Teyssot, and C. Delacourt, "Life prediction methods for lithium-ion batteries derived from a fatigue approach ii. capacity-loss prediction of batteries subjected to complex current profiles," *J. Electrochemical Soc.*, vol. 157 no. 7, pp. A892–A898, 2010.

[18] M. Fleischhammer, T. Waldmann, G. Bisle, B. I. Hogg, and M. Wohlfahrt-Mehrens, "Interaction of cyclic ageing at high-rate and low temperatures and safety in lithium-ion batteries," *J. Power Sources*, vol. 274, pp. 432–439, 2015.

[19] B. Stiaszny, J. C. Ziegler, E. E. Krauß, J. P. Schmidt, and E. Ivers-Tiffée, "Electrochemical characterization and post-mortem analysis of aged LiMn 2 O 4–Li (Ni 0.5 Mn 0.3 Co 0.2) O 2/graphite lithium ion batteries. Part I: Cycle aging," *J. Power Sources*, vol. 251, pp. 439–450, 2014.

[20] N. Lohmann *et al.*, "Cycle life investigations on different li-ion cell chemistries for PHEV applications based on real life conditions (No. 2012-01-0656)," SAE techn. paper, 2012.

[21] A. Barré, F. Suard, M. Gérard, M. Montaru, and D. Riu, "Statistical analysis for understanding and predicting battery degradations in real-life electric vehicle use," *J. Power Sources*, vol. 245, pp. 846–856, 2014.

[22] P. Spagnol, S. Onori, N. Madella, Y. Guezennec, and J. Neal, "Aging and characterization of li-ion batteries in a hev application for lifetime estimation," *IFAC Proc.*, vol. 43 no. 7, pp. 186–191, 2010.

[23] S. T. Mayer, Electric vehicle dynamic-stress-test cycling performance of lithium-ion cells (No. UCRL-ID–116443), Lawrence Livermore National Lab., Livermore, CA, USA, 1994.

[24] K. Morita, M. Akai, and H. Hirose, "Development of cycle life test profiles of lithium-ion batteries for plug-in hybrid electric vehicles," in *Proc. EVS-24*, May 2009, pp. 13–16.

[25] A. Cordoba-Arenas, S. Onori, Y. Guezennec, and G. Rizzoni, "Capacity and power fade cycle-life model for plug-in hybrid electric vehicle lithium-ion battery cells containing blended spinel and layered-oxide positive electrodes," *J. Power Sources*, vol. 278, pp. 473–483, 2015.

[26] A. Dinger *et al.*, "Batteries for electric cars: Challenges, opportunities, and the outlook to 2020," Boston Consulting Group, Boston, MA, USA 2010.

[27] N. Nitta, F. Wu, J. T. Lee, and G. Yushin, "Li-ion battery materials: present and future," *Mater. Today*, vol. 18, no. 5, pp. 252–264, 2015.

[28] Z. Liu, A. Ivanco, and Z. Filipi, "Quantification of drive cycle's rapid speed fluctuations using Fourier analysis," *SAE Int. J. Alternative Powertrains*, vol. 4, pp. 170–177, 2015.

[29] P. Stoica and R. L. Moses, Spectral analysis of signals (Vol. 452).Upper Saddle River, NJ, USA: Pearson/Prentice- Hall 2005.

[30] J. W. Cooley and J. W. Tukey, "An algorithm for the machine calculation of complex fourier series." *Math. Comput.* vol. 19, no. 90, pp. 297–301, 1965.

Authors' photographs and biographies not available at the time of publication.